A Multiactive Bridge Converter With Inherently Decoupled Power Flows

Soumya Bandyopadhyay, *Student Member, IEEE*, Pavel Purgat, *Student Member, IEEE*, Zian Qin, *Senior Member, IEEE*, and Pavol Bauer, *Senior Member, IEEE*

***Abstract*—Multiactive bridge converters (MAB) have become a widely-researched candidate for the integration of multiple renewable sources, storage, and loads for a variety of applications, from robust smart grids to more-electric aircraft. Connecting multiple dc ports reduces power conversion stress, improves efficiency, reduces material billing, and increases power density. However, the power flows between the ports of an MAB converter are magnetically coupled via the high-frequency (HF) transformer, making it difficult to control. This article presents an MAB converter configuration with a rigid voltage source on the magnetizing inductance of the transformer resulting in inherently decoupled power flows. As a result, the configuration allows independent power flow control tuning of the rest of the ports. The theory behind the power flow decoupling of the proposed MAB configuration is analyzed in detail using a reduced-order model. A 2-kW, 100-kHz Si-C-based four-port MAB converter laboratory prototype is built and tested, showing completely decoupled control loops with fast transient response regardless of their control bandwidths. The proposed configuration therefore makes the operation and design of the MAB family of converters much more feasible for any number of ports and precludes the need for a high-performance dynamic decoupling controller.**

***Index Terms*—DC–DC converter, decoupled power flow management, multiactive-bridge converter, multiwinding transformer.**

I. Introduction

MULTIPORT Converters (MPC) have recently gained research attention as a potential solution for versatile energy management systems able to integrate diverse renewable energy sources or conventional energy sources, storage systems, and loads [1]. The advantages of multiport converters are: 1) reduced component requirement; 2) quick dynamic response; 3) high system efficiency and power density; and 4) centralized control. Therefore, multiport converters have many potential applications: 1) more electric aircraft or all-electric ship [2]–[4]; 2) electric vehicle (EV) charging applications [5]–[7]; 3) energy router for smart homes [8]; 4) solid-state transformer (SST) cross-link between medium voltage (MV); and low voltage grid (LV).

The primary purpose of MPCs is to integrate multiple ports with varied voltage and current ratings into a single power stage allowing bidirectional power flow between each port. Apart from bidirectional power flow, specific applications like EV charging also require galvanic isolation between the different ports for safety reasons. Hence, isolated multiport converters are used in those applications by adding a high-frequency (HF) transformer as an intermediate stage [9]. The isolated multiport converter family can be divided into two categories depending on the number of transformers: multiwinding transformer-coupled MPC [9], [10], and multitransformer coupled MPC [11]. One of the promising topologies in the multiwinding transformer-coupled MPC family is the multiactive bridge (MAB) converter. The MAB converter consists of multiple inverter bridges (half-bridge or full-bridge) connected via a high-frequency (HF) multiwinding transformer [8], [9], [12]. Derived from the dual-active bridge (DAB) converter family [13], the MAB converter not only integrates and exchanges the energy from/to all ports but also provides full isolation among all ports and matches the different port voltage levels. Additionally, the MAB converter realizes bidirectional power flow by adjusting the phase-shift angle between the high-frequency ac voltages generated by the inverter module at each port. Fig. 1 shows the topology of a generic n-port MAB converter.

A key challenge in the design and control of the MAB converter is the inherent cross-coupling of power flows between ports due to the interwinding magnetic coupling of the transformer. Therefore, the MAB converter behaves as a multiinput–multioutput (MIMO) system with coupled power loops, which is difficult to control. In literature, several control techniques to decouple the power flows are reported. The main goal of these techniques is to simplify the cross-coupled MIMO control loops into multiple independent single-input–single-output (SISO) control loops. A feedforward compensator-based control method is proposed in [14], which decouples the control loops dynamically with precalculated decoupling matrices stored as a look-up table in the controller. Another control technique decouples the control loops by choosing different bandwidths for the SISO loops [8], [15], [16]. Therefore, the loop with the highest bandwidth determines the phase-shift direction during transients. A hybrid approach combining the above two methods is reported

Manuscript received November 18, 2019; revised March 1, 2020, April 28, 2020, and June 10, 2020; accepted June 21, 2020. Date of publication July 1, 2020; date of current version September 22, 2020. This work was supported by Research Programme P 13-21 with Project No. A funded by the Netherlands Organisation for Scientific Research (NWO). Recommended for publication by Associate Editor Y. Siwakoti. *(Corresponding author: Zian Qin.)*

The authors are with the Department of Electrical Sustainable Energy, DCE&S group, TU Delft, 2628 CD Delft, The Netherlands (e-mail: s.bandyopadhyay-1@tudelft.nl; p.purgat@tudelft.nl; z.qin-2@tudelft.nl; p.bauer@tudelft.nl).

Color versions of one or more of the figures in this article are available online at https://ieeexplore.ieee.org.

Digital Object Identifier 10.1109/TPEL.2020.3006266

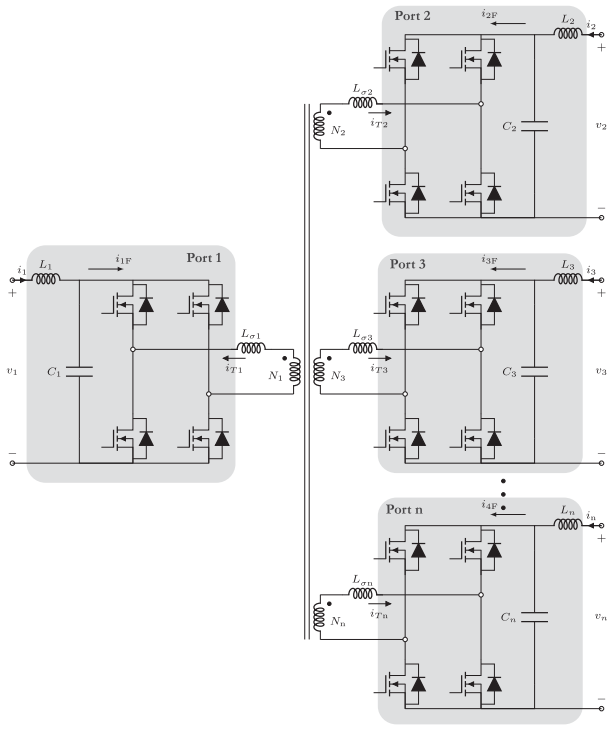

Fig. 1. Topology of an MAB converter.

in [4] for applications like more-electric aircraft (MEA) to integrate storage systems with different dynamic behavior. A time-sharing control strategy is reported in [12] and [17], which decouples the power flows by operating the MAB converter as a DAB converter with only two active ports and other ports deactivated as diode rectifiers at any particular time period. However, the device stress and the voltage ripple associated with this control technique are usually high, which leads to larger filtering capacitors. All the abovementioned control techniques are challenging to implement due to their complexity. Thus, they inhibit the scalability of the number of ports in MAB converters and reduces their applicability. The authors in [18] propose a hardware decoupling approach by adding a capacitor to create a series resonant port in the multiport converter. However, the approach uses an additional passive power device which results in higher losses and results in lower efficiency.

This article proposes a modified configuration of the MAB converter, which leads to inherently decoupled power flows. Typically MAB converters (see Fig. 1) use external inductors as leakage inductances in addition to transformer leakage inductances to control power flow. In the proposed configuration, the HF transformer is optimally designed to ensure a low leakage inductance in one port (master) without an external inductor and a relatively higher leakage inductance in the rest of the ports (slave) by adding an external inductor. This feature results in the near decoupling of the individual power flow between the slave ports, making the low leakage inductance port or the master port the same as the slack bus. Due to the decoupling inherent to the proposed MAB configuration, the multivariable coupled control system is decomposed into a series of independent single-loop subsystems, which avoids the need for advanced control methods. As a result, high bandwidth for each control loop and rapid dynamic response can be achieved independently. In addition, due to simple control requirements, this configuration enables the scalability of the number of ports without increasing any control complexity. Further, the proposed configuration uses one less power device, which results in lower losses and leads to higher efficiencies. A reduced-order dynamic model of MAB converters is used to analyze the decoupling of the MAB converter and its boundaries. A 2-kW, 100-kHz, Si-C-based prototype of a four-port multiactive bridge converter or a quad-active bridge converter (QAB) is built and successfully tested. The experimental results confirm the theoretical analysis and show the inherent decoupling and fast dynamic response. In summary, the main contributions of this article compared to previous works are as follows:

1) introduce a hardware-based solution to the inherent coupling problem of MAB converters without adding extra hardware;
2) derive design thumb rules to achieve near decoupling using an asymmetrical distribution of leakage inductances;
3) show that it is easier to determine the soft-switching boundaries of the individual ports since their transformer current shapes are like DAB converters;
4) present in-depth analysis of the distribution of losses in the proposed asymmetric four-port MAB converter with experimental validation.

Furthermore, extensive experimental validation of the proposed decoupling approach is presented, which shows power flows in the MAB converter ports are controlled independently regardless of controller bandwidth. Experiments also demonstrate the bidirectional power flow capability of MAB converters.

The article is organized into six parts. The theory of the MAB converter along with the analysis of the power flow coupling are reviewed in Section II. Based on the previous analysis, Section III presents a decoupled MAB converter along with an in-depth study on the operating boundaries of decoupling. Simulations on a four-port MAB converter or a quad-active bridge converter (QAB) are discussed in Section IV. Section V reports the experimental results on the QAB converter laboratory prototype. Finally, general conclusions are summarized based on the analysis and the results in Section VI.

II. Theory of MAB Converter

A. MAB Equivalent Power Flow Circuit and Waveforms

Fig. 1 presents the topology of an *n*-port MAB converter comprised of *n* full-bridge modules magnetically coupled via an *n*-winding HF transformer. A star-equivalent model (see Fig. 2) is used for analysing the operation and switching conditions of the MAB converter. The ports of the MAB converter in Fig. 1 are replaced by rectangular voltages sources in the equivalent circuit. For convenience, the magnetizing inductance L_{m}, the leakage inductances $L_{\sigma\mathrm{k}}$ and the generated ac voltages and ac

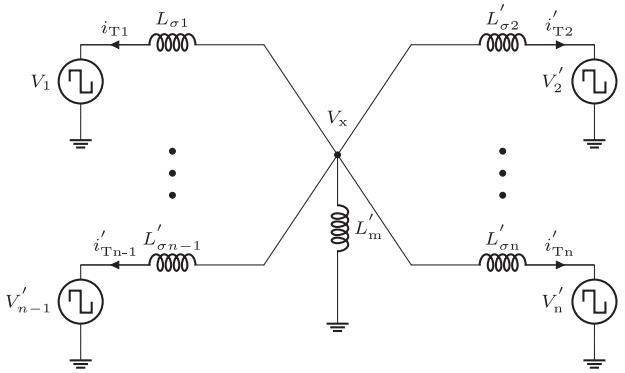

Fig. 2. Star-equivalent model of an MAB topology.

currents are referred to port #1

$$V_{\mathrm{k}}^{'} = \frac{N_1}{N_{\mathrm{k}}} V_{\mathrm{k}}, \quad i_{\sigma \mathrm{k}}^{'} = \frac{N_{\mathrm{k}}}{N_1} i_{\sigma \mathrm{k}}, \quad L_{\sigma \mathrm{k}}^{'} = \left(\frac{N_1}{N_{\mathrm{k}}}\right)^2 L_{\sigma \mathrm{k}}. \tag{1}$$

The expression for voltage at the star-point (V_{x}) is obtained by applying theory of superposition to estimate the Thevenin voltage contribution of all the ports

$$V_{\mathrm{x}} = \sum_{\mathrm{i}=1}^{n} \frac{\left(\sum_{\mathrm{j}=1,\mathrm{j}\neq \mathrm{i}}^{n} \frac{1}{L'_{\sigma \mathrm{j}}}\right)^{-1}}{L'_{\sigma \mathrm{i}} + \left(\sum_{\mathrm{j}=1,\mathrm{j}\neq \mathrm{i}}^{n} \frac{1}{L'_{\sigma \mathrm{j}}}\right)^{-1}} V_{\mathrm{i}}^{'}. \tag{2}$$

Therefore, the current slopes of the transfomer windings of the MAB equivalent circuit can be expressed as the following:

$$\frac{di_{\mathrm{Ti}}^{'}}{dt} = \frac{V_{\mathrm{x}} - V_{\mathrm{i}}^{'}}{L'_{\sigma \mathrm{i}}}. \tag{3}$$

The actual transformer currents can be obtained by integrating (3) over a switching period. The shape of the transformer currents is dependent on the type of modulation strategy used to modulate the star-point voltage V_{x}. Classically single phase-shift modulation strategy (SPS) is applied to most MAB converter solutions [8], [19]. According to the operating principles of SPS modulation, the MAB bridges generate the square-wave voltages V_{i} with a 50% duty, and the phase shift ϕ_{ij} between the driving signals for the bridges determines the power level and direction. Fig. 3 shows the idealized transformer waveforms of a four-port MAB converter with SPS modulation strategy.

B. Power Flow and Link Inductances

MAB converter is a natural extension of the dual-active bridge (DAB) converter introduced in [13]. A DAB converter can be considered as an MAB converter with two active ports. Therefore, the power flow equations derived for DAB converters can be extended to an MAB converter. The cycle-to-cycle average power transferred between port #i and port #j of an MAB converter is given by

$$P_{\mathrm{ij}} = \frac{V_{\mathrm{i}}^{'} V_{\mathrm{j}}^{'}}{2\pi f_{\mathrm{s}} L_{\mathrm{ij}}} \phi_{\mathrm{ij}} \left(1 - \frac{|\phi_{\mathrm{ij}}|}{\pi}\right), \qquad \phi_{\mathrm{ij}} = \phi_{\mathrm{i}} - \phi_{\mathrm{j}} \tag{4}$$

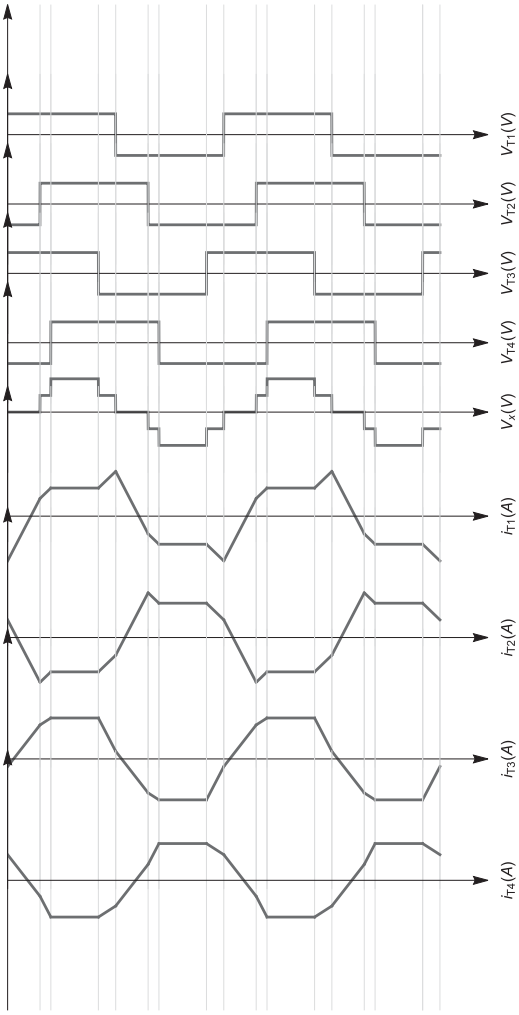

Fig. 3. Idealized steady-state switching waveforms for unity-dc-conversion ratios and equal leakage inductances of a four-port MAB converter or a QAB converter.

where $V_{\mathrm{i}}^{'}$ and $V_{\mathrm{j}}^{'}$ are the port dc voltages; L_{ij} is the equivalent inductance between ports #i and #j; f_{s} is the switching frequency; and ϕ_{ij} is the phase-shift between the two square wave voltages at the corresponding transformer terminals. It is evident from (4) that to compute the power flow between ports #i and #j the equivalent inductance (L_{ij}) between two ports need to be calculated. The star-equivalent circuit of MAB converters is already introduced in the previous section. However, the effective inductance between two ports is not readily obtained from the star representation. Therefore, a delta MAB equivalent power flow model as shown in Fig. 4 is required to analyze the power flow between ports. The MAB delta power flow model represents point-to-point DAB power flow between any two ports of an MAB converter.

Theory of superposition is applied on the star-equivalent model to obtain the delta power flow model. The Thevenin-equivalent inductance between any two ports #i and #j represented as L_{ij} is obtained by applying the theory of superposition on the star-equivalent circuit, as shown in Fig. 2. Accordingly, all the remaining voltage sources are shorted, resulting in the circuit

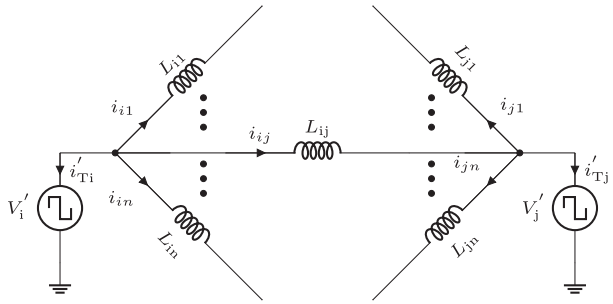

Fig. 4. Delta power flow model of MAB converter topology.

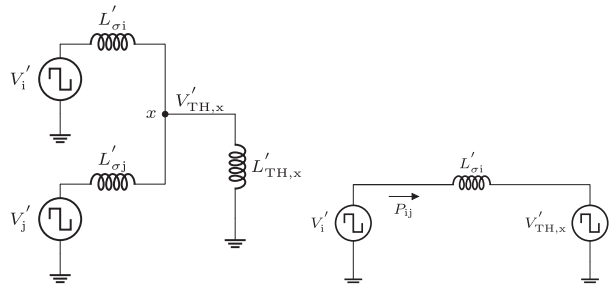

Fig. 5. (a) Thevenin-equivalent impedance of the rest of the ports with the voltage sources short-circuited. (b) Obtained Thevnin-equivalent circuit of port #i with respect to star-point x with the Thevenin voltage contribution of port j.

shown in Fig. 5(a). The Thevenin inductance ($L_{\mathrm{TH,x}}$) between the rest of the circuit and the star-point is the parallel combination of leakage inductance of the remaining ports and the transformer magnetizing inductance

$$L'_{\mathrm{TH,x}} = \left(\frac{1}{L'_{\mathrm{m}}} + \sum_{k\neq i,j}^{n} \frac{1}{L'_{\sigma \mathrm{k}}}\right)^{-1} \simeq \left(\sum_{k\neq i,j}^{n} \frac{1}{L'_{\sigma \mathrm{k}}}\right)^{-1}. \quad (5)$$

Furthermore, it is assumed that the transformer magnetizing inductance is significantly higher than the leakage inductances of the port windings. The Thevenin equivalent ac voltage $V_{\mathrm{TH,x}}$ at the star port can be obtained as the superposition of voltages from ports #i and #j

$$V'_{\mathrm{TH,x}} = \left(\frac{L'_{\sigma \mathrm{i}} \| L'_{\mathrm{TH,x}}}{L'_{\sigma \mathrm{i}} + L'_{\sigma \mathrm{i}} \| L'_{\mathrm{TH,x}}}\right) V'_{\mathrm{i}} + \left(\frac{L'_{\sigma \mathrm{j}} \| L'_{\mathrm{TH,x}}}{L'_{\sigma \mathrm{j}} + L'_{\sigma \mathrm{j}} \| L'_{\mathrm{TH,x}}}\right) V'_{\mathrm{j}}. \quad (6)$$

Since the active power transfer from $V'_{\mathrm{TH,x}}$ to the ground is zero, the active power transfer between port #i and port #j is equal to the active power transfer between port #i and $V'_{\mathrm{TH,x}}$ resulting the DAB equivalent circuit between port #i and star-point x as seen in Fig. 5(b). Therefore, applying the DAB power flow equation (4) between V'_{i} and $V'_{\mathrm{TH,x}}$, the active power can be written as

$$P_{\mathrm{ij}} = \frac{V'_i V'_{\mathrm{TH,x}}}{2\pi f_{\mathrm{s}} L'_{\sigma \mathrm{i}}} \phi_{\mathrm{ij}} \left(1 - \frac{|\phi_{\mathrm{ij}}|}{\pi}\right). \quad (7)$$

Further, it must be noted that while computing the power flow between port #i and star-point x, the voltage contribution of V'_{i} in $V'_{\mathrm{TH,x}}$ will not result in active power flow since it is in phase with itself. Therefore, substituting only the contribution of V'_{j} in (6) into (7), the generic power flow equation between the two ports in an MAB converter can be derived as

$$P_{\mathrm{ij}} = \frac{V'_{\mathrm{i}} V'_{\mathrm{j}}}{2\pi f_{\mathrm{s}} \left(L'_{\sigma \mathrm{i}} + L'_{\sigma \mathrm{j}} + \dfrac{L'_{\sigma \mathrm{i}} L'_{\sigma \mathrm{j}}}{L'_{\mathrm{TH,x}}}\right)} \phi_{\mathrm{ij}} \left(1 - \frac{|\phi_{\mathrm{ij}}|}{\pi}\right). \quad (8)$$

Therefore, comparing (8) to the DAB power flow form (4) and combining with (5), the link inductance L_{ij} between ports #i and #j can be formulated as

$$L_{\mathrm{ij}} = \begin{cases} \mathrm{NA}, & \forall i = j \\ L'_{\sigma \mathrm{i}} + L'_{\sigma \mathrm{j}} + L'_{\sigma \mathrm{i}} L'_{\sigma \mathrm{j}} \left(\sum_{k\neq i,j}^{n} \dfrac{1}{L'_{\sigma \mathrm{k}}}\right), & \forall i \neq j. \end{cases} \quad (9)$$

Based on that, the inherent coupling between the power flow between ports is analyzed. The power flow coupling of the MAB converter can be investigated by the star-equivalent circuit as shown in Fig. 2.

C. Small Signal Model and Control of MAB Converter

Analyzing the controllability of the MAB system requires a small signal model describing the relationship between the control inputs and outputs. Generally, state-space averaging technique is used to model the dynamic behavior of dc–dc converters [20], [21]. However, in the case of isolated dc–dc converters like the MAB converter, one of the state-variable is the transformer current, which does not satisfy the small-ripple approximation [22]–[24]. Since the power flow coupling can be analyzed by low-frequency dynamics, the influence of the high-frequency leakage inductor dynamics of the transformer can be neglected [8], [14], [25]. To that end, an approximate control-oriented small signal system model can be derived by linearizing the system at a dc operating point. The currents at different ports of the MAB converter before the dc side filters, as shown in Fig. 1 can be expressed in equation form in the following:

$$i_{\mathrm{Fi}} = \frac{P_{\mathrm{i}}}{V_{\mathrm{i}}} = \frac{\sum_{j\neq i}^{n} P_{\mathrm{ij}}}{V_{\mathrm{i}}}, \qquad \forall i \in (1, n). \quad (10)$$

Combining (10) with (4) the following expression for the ith port current is obtained

$$i_{\mathrm{Fi}} = \sum_{j\neq i}^{n} \frac{V_{\mathrm{j}}}{2\pi f_{\mathrm{s}} L_{\mathrm{ij}}} f(\phi_{\mathrm{ij}}), \quad \forall i \in (1, n) \quad (11)$$

where $f(\phi)$ is a nonlinear function of the control variables defined as following based on power flow (8):

$$f(\phi_{\mathrm{ij}}) = f(\phi_{\mathrm{i}} - \phi_{\mathrm{j}}) = \phi_{\mathrm{ij}} \left(1 - \frac{|\phi_{\mathrm{ij}}|}{\pi}\right). \quad (12)$$

Since the state variables or port currents are a nonlinear function of the control inputs, the system needs to be linearzied at a dc operating point. The nominal plant is assumed to be lossless, and only the predominant dynamics associated with the filters at the dc side of each port have been considered herein. The Taylor

series expansion of above port currents at an operating point A is

$$I_i = I_{\mathrm{i,A}} + \Delta I_{\mathrm{i,A}} \tag{13}$$

$$\Delta I_{\mathrm{i,A}} = \sum_{j\neq i}^{n} G_{\mathrm{ij}} \Delta\phi_{\mathrm{ij}}, \qquad \forall \mathrm{i} \in (1,n) \tag{14}$$

$$G_{\mathrm{ij}} = \frac{\partial I_{\mathrm{i,A}}}{\partial \phi_{\mathrm{ij}}} \qquad \forall \mathrm{i} \in (1,n). \tag{15}$$

Since it is always the phase shift between the ports that enable the power transfer, to simplify the control, the phase of port one can be fixed to be zero. Therefore, the small signal gain matrix of the MAB converter can be expressed as

$$\Delta\mathbf{I} = \begin{bmatrix} \Delta I_2 \\ \Delta I_3 \\ : \\ \Delta I_{\mathrm{i}} \\ : \\ \Delta I_{\mathrm{n}} \end{bmatrix} = \begin{bmatrix} G_{22} & G_{23} & .. & .. & G_{2n} \\ G_{32} & G_{33} & .. & .. & G_{3n} \\ : & : & .. & .. & : \\ G_{\mathrm{i2}} & G_{\mathrm{i3}} & .. & .. & G_{\mathrm{in}} \\ : & : & .. & .. & : \\ G_{\mathrm{n2}} & G_{\mathrm{n3}} & .. & .. & G_{\mathrm{nn}} \end{bmatrix} \begin{bmatrix} \Delta\phi_2 \\ \Delta\phi_3 \\ : \\ \Delta\phi_{\mathrm{i}} \\ : \\ \Delta\phi_{\mathrm{n}} \end{bmatrix}$$

$$= \mathbf{G}\boldsymbol{\Delta}\phi \tag{16}$$

where the expressions of the gain elements $G_{\mathbf{ij}}$ $\forall[i,j]$ in the matrix can be expressed as

$$G_{\mathrm{ij}} = \begin{cases} \sum_{p\neq i}^{n} \dfrac{V_{\mathrm{p,A}}}{2\pi f_{\mathrm{s}} L_{\mathrm{ip}}} \left(1 - \dfrac{2|\phi_{\mathrm{i,A}} - \phi_{\mathrm{p,A}}|}{\pi}\right), & \forall[i=j] \\ -\dfrac{V_{\mathrm{j,A}}}{2\pi f_{\mathrm{s}} L_{\mathrm{ij}}} \left(1 - \dfrac{2|\phi_{\mathrm{j,A}} - \phi_{\mathrm{i,A}}|}{\pi}\right), & \forall[i\neq j]. \end{cases} \tag{17}$$

Since G_{ij} $\forall[i,j]$ are all nonzero entities, the resulting control input to output gain matrix $\mathbf{G}$ becomes a nondiagonal matrix. The ratio of the nondiagonal terms G_{ij} $\forall[i\neq j]$ to the diagonal elements of the gain matrix $\mathbf{G}$ represents the degree of cross-coupling between the individual control loops [26]. This concludes the mathematical analysis to quantify the power flow coupling of MAB converters.

III. MAB Converter Configuration With Inherently Decoupled Power Flow

A modified configuration of the MAB is proposed and described in detail in this section, which inherently decouples interport flows. The small-signal model developed in Section II-C is applied to investigate the degree of the cross-coupling associated with the proposed configuration. Finally, a qualitative comparison between the proposed solution and the existing solution reported in the literature.

Section II showed that the interport MAB power flow is dependent on the leakage inductance associated with the individual ports. The leakage inductances can be realized by incorporating them into the design of the multiwinding transformer. This approach, however, results in higher losses in the transformer. As a result, the leakage inductances are realized by adding external inductors to the windings of the transformer, resulting in higher design flexibility [8], [14]. Fig. 6 presents the star-equivalent

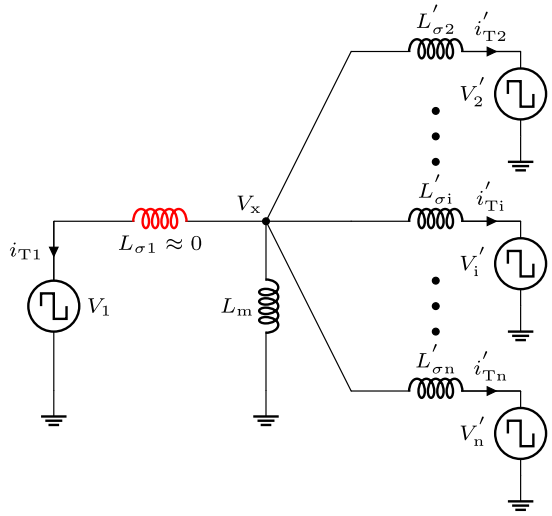

Fig. 6. Star-equivalent circuit of the proposed MAB converter configuration with port #1 as the master port, i.e, $L_{\sigma 1} \approx 0$.

model of the proposed MAB configuration based on external leakage inductors. Compared to the conventional MAB configuration (see Fig. 1), an external leakage inductor of one of the ports is omitted. This port is referred to as the "master" port and all other ports are referred to as the "slave port." Depending on the application, a stiff-voltage source like a grid or a battery should be connected to the master port. Since the leakage inductance of the master port transformer winding is significantly lower than the slave ports, it essentially regulates the voltage across the magnetizing impedance transformer, thus decoupling the power flow between the slave ports. However, the "master" port leakage inductance is not zero in practical applications. The winding of the transformer linked to the master port has its own leakage inductance. A sensitivity analysis of the "master" port leakage inductance on the dynamic decoupling performance of the control loops is conducted in Section IV. Section V discusses the practical implementation of such transformer.

A. Equivalent Circuit and Waveforms

Fig. 6 shows the star-equivalent circuit of the proposed configuration. Similar to the analysis presented in Section II-A, the voltage at the star-point (V_{x}) and the current slopes of the transfomer windings of the proposed MAB converter can be expressed as the following:

$$V_{\mathrm{x}} = V_1 \tag{18}$$

$$\frac{di'_{\mathrm{Ti}}}{dt} = \frac{V_1 - V'_{\mathrm{i}}}{L'_{\sigma \mathrm{i}}}, \qquad \forall i \in [2,n]. \tag{19}$$

The inductor currents of the ports of the proposed MAB converter can be obtained by integrating (19). Fig. 7 shows the idealized waveforms of a four-port MAB converter with a null-leakage inductor at port #1. Comparing the waveforms in Fig. 7 to the conventional MAB converter waveforms in Fig. 3, it can be observed that the shape of the slave port inductor currents ($i'_{\mathrm{T2}}, i'_{\mathrm{T3}}, i'_{\mathrm{T4}}$) are trapezoidal in nature similar to a DAB

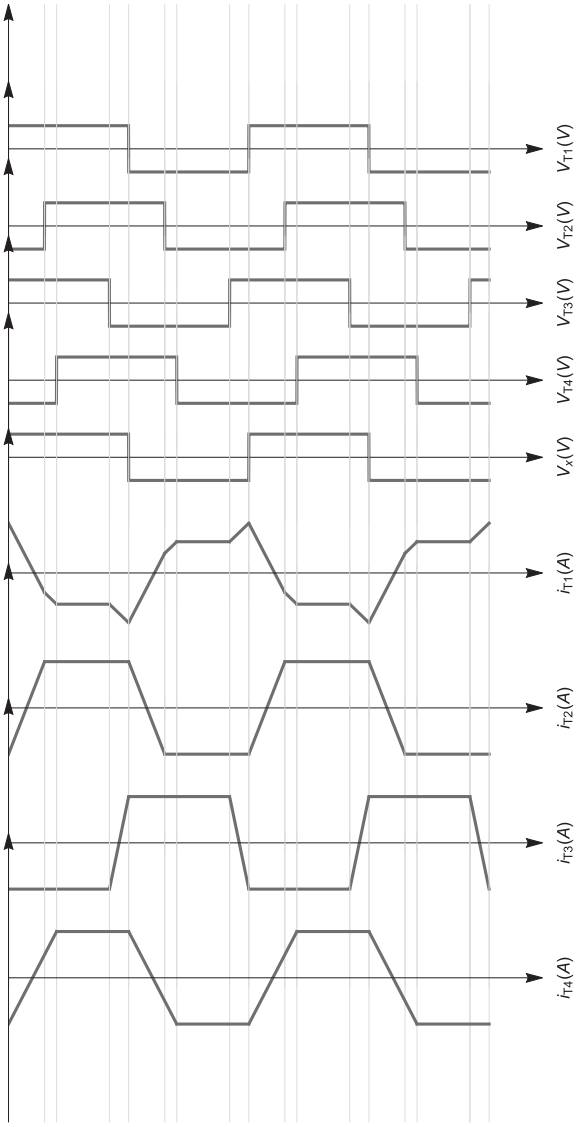

Fig. 7. Idealized steady-state switching waveforms for unity-dc-conversion ratios and equal link inductances of the proposed four-port MAB converter.

converter. However, the master port inductor current (i_{T1}) is not trapezoidal since it is a superposition of the all the trapezoidal slave port inductor currents.

Since the slave port transformer currents are essentially similar to that of DAB converters, all modulation strategies applicable to DAB converters like trapezoidal modulation (TZM), triangular modulation (TRM), and hybrid methods can be applied to improve efficiency. Additionally, the soft switching boundaries of the ports are independent of the operating points of the other ports. Therefore, it is easier to design duty-cycle-based soft-switching control of the proposed low leakage port MAB configuration [14], [16].

B. Link Inductances and Power Flow

The proposed MAB configuration is a special case of the conventional configuration with the leakage inductance of the master port reduced removed. Rewriting the link inductance expression L_{ij} of (9) with selecting port #1 as the master port, i.e, $L_{\sigma 1} \approx 0$

$$L_{\mathrm{ij}} = \begin{cases} \mathrm{NA}, & i = j \\ L_{\sigma \mathrm{j}}^{'}, & i = 1, j \neq 1 \\ L_{\sigma \mathrm{i}}^{'}, & i \neq 1, j = 1 \\ \infty, & i \neq 1, j \neq 1, i \neq j. \end{cases} \tag{20}$$

Therefore, the generic power flow equation for the proposed configuration can be subdivided into two cases: 1) power flow equation between the master port and any slave port, and 2) power flow between any two slave ports

$$P_{\mathrm{ij}} = \begin{cases} 0, & i \neq 1, \forall j \in [2, n] \\ 0, & j \neq 1, \forall i \in [2, n] \\ \dfrac{V_{\mathrm{i}}^{'} V_{\mathrm{j}}^{'}}{2\pi f_{\mathrm{s}} L_{\mathrm{ij}}} \phi_{\mathrm{ij}} \left(1 - \dfrac{|\phi_{\mathrm{ij}}|}{\pi}\right), & i = 1, \forall j \in [2, n] \\ \dfrac{V_{\mathrm{i}}^{'} V_{\mathrm{j}}^{'}}{2\pi f_{\mathrm{s}} L_{\mathrm{ij}}} \phi_{\mathrm{ij}} \left(1 - \dfrac{|\phi_{\mathrm{ij}}|}{\pi}\right), & j = 1, \forall i \in [2, n]. \end{cases} \tag{21}$$

Based on the power flow equation derived for the proposed MAB configuration, a small signal model is developed in the following section.

C. Small Signal Model and Controllability

The prefiltered currents at different ports of the proposed MAB converter can be expressed in equation form in the following:

$$i_{\mathrm{Fi}} = \begin{cases} \dfrac{\sum_{j \neq i}^{n} P_{\mathrm{ij}}}{V_{\mathrm{i}}}, & i = 1 \\ \dfrac{P_{\mathrm{i1}}}{V_{\mathrm{i}}}, & i \neq 1, i \forall \in [2, n]. \end{cases} \tag{22}$$

Combining the above equations with the power flow equation (4), they can be expressed as the following:

$$i_{\mathrm{Fi}} = \begin{cases} \sum_{j \neq i}^{n} \dfrac{V_{\mathrm{j}}}{2\pi f_{\mathrm{s}} L_{\sigma \mathrm{j}}} f(\phi_{\mathrm{i}} - \phi_{\mathrm{j}}), & i = 1 \\ \dfrac{V_1}{2\pi f_{\mathrm{s}} L_{\sigma \mathrm{j}}} f(\phi_1 - \phi_{\mathrm{i}}), & \forall i \in [2, n]. \end{cases} \tag{23}$$

Since the port #1 is selected as the "master" port, it acts as the slack bus and the phase shift of this port is fixed at 0. The phase shifts of the slave ports are used to control their respective currents. Linearizing the system at a certain operating point A, and applying the Taylor series expansion of above port currents as carried out previously in (13)–(15) the small signal gains from input (ϕ_2, ..., ϕ_{n}) to output (i_2, ..., i_{n}) can be derived as following:

$$G_{\mathrm{ij}} = \begin{cases} 0, & \forall [i \neq j] \\ \dfrac{V_{1,\mathrm{A}}}{2\pi f_{\mathrm{s}} L_{\sigma \mathrm{i}}} \left(1 - \dfrac{2|\phi_{\mathrm{i,A}} - \phi_{1,\mathrm{A}}|}{\pi}\right), & \forall [i = j] \in [2, n]. \end{cases} \tag{24}$$

TABLE I
OVERVIEW OF MAB DECOUPLING STRATEGIES

Performance metrics	Software control solution			Hardware solution	
	Inverse matrix compensator [4], [14]	Band decoupling [15], [16]	Time-sharing [12]	Series-Resonant Capacitor [18]	Proposed Configuration
Computational effort or data storage	High	Low	Low	Low	Low
Controller architecture	Centralized	Decentralized	Centralized	Decentralized	Decentralized
Hardware design complexity/constraint	Low	Low	Medium	Medium	High
Additional component	-	-	-	One extra capacitor	One less inductor

Therefore, the small signal gain matrix of the proposed MAB converter configuration can be expressed as

$$\Delta \mathbf{i} = \begin{bmatrix} \Delta i_2 \\ \Delta i_3 \\ : \\ \Delta i_{\mathrm{i}} \\ : \\ \Delta i_n \end{bmatrix} = \begin{bmatrix} G_{22} & 0 & .. & .. & 0 \\ 0 & G_{33} & .. & .. & 0 \\ : & : & .. & .. & : \\ 0 & 0 & .. & G_{ii} & 0 \\ : & : & .. & .. & : \\ 0 & 0 & .. & .. & G_{nn} \end{bmatrix} \begin{bmatrix} \Delta \phi_2 \\ \Delta \phi_3 \\ : \\ \Delta \phi_i \\ : \\ \Delta \phi_n \end{bmatrix} = \mathbf{G} \mathbf{\Delta} \phi. \quad (25)$$

It can be observed that the small-signal gain matrix of the proposed configuration is a diagonal matrix with all the nondiagonal elements approaching zero. Therefore, there is no cross-coupling between the control loops.

Compared to existing solutions for the power flow decoupling in literature, the proposed MAB configuration has several advantages. The main advantage of the proposed architecture is that it is essentially decomposing a tightly coupled MIMO network into multiple independent SISO systems. On the other hand, some of the solutions published in the literature concentrate at solving the problem of MIMO coupling in the control domain, leading to sophisticated but complex control strategies. The authors in [4] and [14] uses precalculated decoupling matrices to decouple the power flows. Excellent dynamic decoupling performance has been documented using this technique. However, the control strategies mentioned have a high cost of computation or digital storage and therefore require powerful DSPs. In addition, with an increasing number of ports, the complexity of the decoupling controller is further increasing, which hinders scalability. Another control technique decouples the control loops by choosing different bandwidths for the SISO loops [8], [15], leading to relatively simpler control implementation. The port with the highest bandwidth responds the quickest during transient operation. The scalability of ports with this strategy is more feasible than the previous solutions based on advanced control. However, decoupling performance is not optimal since the disturbance created by the control action of the fast loops might affect the slower control loops. Additionally, the controllability of the system is not adequate since there are restrictions on the choice of control bandwidths for different ports. A time-sharing control strategy is proposed in [12], which decouples the power flows by operating the MAB converter as a DAB converter with only two active ports and other ports deactivated as diode rectifiers at any particular time period. Control is comparatively simpler to the decoupling matrix approach. However, inherently, this strategy suffers from a slow transient response and high device stresses. Therefore, it is not suitable for applications requiring fast control and high efficiency. The authors in [18] propose adding a capacitor in series with the leakage inductance to ensure low impedance port resulting in hardware decoupling. However, the approach uses an extra power device which reduces efficiency and limits applicability at high power solutions. Table I presents a summary of the qualitative comparison of the proposed hardware solution to the current MAB power flow decoupling strategies which approach the problem from both a control and hardware perspective.

IV. SIMULATIONS ON A QAB CONVERTER

Simulations on a four-port MAB converter or a QAB converter are carried out and analyzed in this section to validate the theoretical considerations presented in the previous section. Initially, the QAB converter specifications and control strategy considered in the simulation are discussed. The selected simulation package is MATLAB/Simulink augmented with the PLECS blockset. A detailed analysis of the results obtained from the simulations is presented at the end of this section.

A. QAB Converter Specifications and Control Strategy

The QAB converter schematic used for the simulation study is presented in Fig. 8. The converter is comprised of four ports: Three bidirectional voltage ports, and a load port consisting of a resistor in parallel with a capacitor. The voltage sourced port #1 is used as the "master port" as introduced in Section III which acts as the slack bus of the multiport converter. Table II presents the simulation parameters of the different ports of the QAB converter. The base inductance L_{base} value is obtained by using the maximum power flow equation between two ports of an MAB converter when $\phi_{\mathrm{ij}} = \dfrac{\pi}{2}$ resulting in the following expression:

$$P_{\mathrm{rated}} = \frac{V_{\mathrm{rated}}^2}{8 f_{\mathrm{sw}} L_{\mathrm{base}}}. \quad (26)$$

TABLE II
QAB CONVERTER SPECIFICATIONS

Description	Symbol	Unit	Port			
			#1	#2	#3	#4
Voltage rating	V_{rated}	V	200	200	200	160
Current rating	I_{rated}	A	10	10	10	10
Leakage inductance	L_σ	pu	0	1	1	1
LC filter inductance	L_{f}	μH	3	3	3	3
LC filter capacitance	C_{f}	μF	500	500	500	100
Phase-shift angle range	ϕ	rad	0	$-\frac{\pi}{2}$ to $\frac{\pi}{2}$	$-\frac{\pi}{2}$ to $\frac{\pi}{2}$	0 to $\frac{\pi}{2}$
Switching frequency	f_{sw}	kHz	100	100	100	100

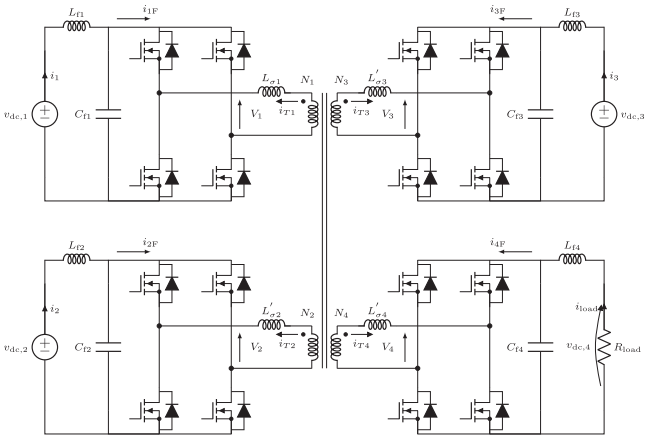

Fig. 8. QAB converter schematic for simulation. Port #1, port #2, and port #3 are connected with a voltage source and port #4 is connected with an RC load.

Using the values of switching frequency, rated power, and rated voltage from the QAB converter specifications in Table II in revised manuscript, the base inductance L_{base} results in 25 μ.

In the control system, there are three control loops: Two current loops for the bidirectional voltage sources in ports #2 and #3; and a voltage control loop for the resistive load in port #4 with $R_{\text{load}} = 35\ \Omega$. Therefore, the voltage source in port #1 acts as the "master" port or the slack bus. Simple phase shift control is used to control the QAB converter. Fig. 9(a) shows the block diagram of the QAB control system. The PI controller for the voltage loop is designed to be slower than the current loops to investigate the interactions between the individual loops. For the current control, a crossover frequency of 1.5 kHz is selected, while for the load voltage control only 10 Hz is chosen as shown in the open loop bode plots Fig. 9(b) and (c). The small signal gain matrix for MAB converters derived in (16) can be rewritten for the QAB converter

$$\begin{bmatrix} \Delta i_{2\text{F}} \\ \Delta i_{3\text{F}} \\ \Delta i_{4\text{F}} \end{bmatrix} = \begin{bmatrix} G_{22} & G_{23} & G_{23} \\ G_{32} & G_{33} & G_{34} \\ G_{42} & G_{43} & G_{44} \end{bmatrix} \begin{bmatrix} \Delta\phi_2 \\ \Delta\phi_3 \\ \Delta\phi_4 \end{bmatrix} \tag{27}$$

where i_{iF} (i $\in [1, 4]$) are the prefilter currents of the dc ports. The dynamics of the dc port currents (i_{i}) can be obtained combining (27) with the transfer functions of the dc side filters of the QAB ports which are defined as

$$G_{1\text{I}}(s) = \frac{\Delta i_2}{\Delta i_{2\text{F}}}, \quad G_{2\text{I}}(s) = \frac{\Delta i_3}{\Delta i_{3\text{F}}}, \quad G_{\text{VI}}(s) = \frac{\Delta V_{\text{dc,4}}}{\Delta i_{4\text{F}}}. \tag{28}$$

B. Results and Discussion

The goal of the simulations is to prove the effectiveness of the proposed converter configuration in terms of decoupling the power flows to gain precise and independent control on the individual ports. To that end, two case studies are considered.

1) Case study I: Load step in the resistive load port #4 to investigate the effect of the relatively slower voltage loop on the faster current loops.
2) Case study II: Simultaneous step change of current reference points in the current controlled ports #2 and #3 to study the effect of the faster current loops on the efficacy of the voltage control loop.

In addition, simulations were performed of various leakage inductances in the master port to test the sensitivity analysis of the degree of the control loop decoupling. The simulations are carried out at the following operating point: $P_{\text{load,4}} = -700$ W; $P_2 = 800$ W; $P_3 = -800$ W. At this operating point, the QAB converter acts in the 2 source–2 load configuration (2S-2 L) with ports #1 and #2 as the sources and ports #3 and #4 as the loads. The obtained simulation results are analyzed in the following.

Case Study I: The load step is realized by switching a resistor of $R_{\text{sw}} = 130\ \Omega$ across the existing load resistor R_{load}. Fig. 10(a) presents the dynamic performance of the current loops and voltage loops of the ports during the load step in the load port at a certain instant (t = 0.11 s). It is noted that the voltage restoration control during the load step has no major effect on the current loops in ports #2 and #3, which are capable of holding currents at their set-points irrespective of the master port leakage inductance. As the current loops are much faster than the voltage loop, they reject the interference independently of the leakage inductance of the master port. However, the dynamic performance of the load port voltage loop deteriorates with increasing leakage inductance in the master port which is observed in the 12.5% drop of the nominal voltage when $L_{\sigma 1} =$ 0.8 pu compared to only 7% drop when $L_{\sigma 1} = 0.04$ pu. The increasing leakage inductance of the master port increases the effective inductance between the load port and the master port,

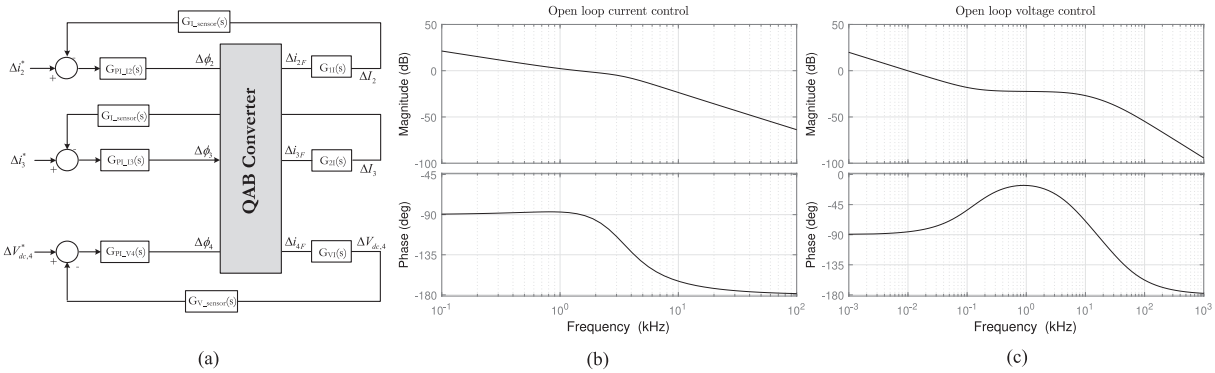

Fig. 9. (a) Block diagram of the QAB control system with three control loops: Port #2 current control loop, port #3 current control loop, and port #4 voltage control loop. (b) Open loop response of current control loops of ports #2 and #3. (c) Open loop response of voltage control loop of port #4.

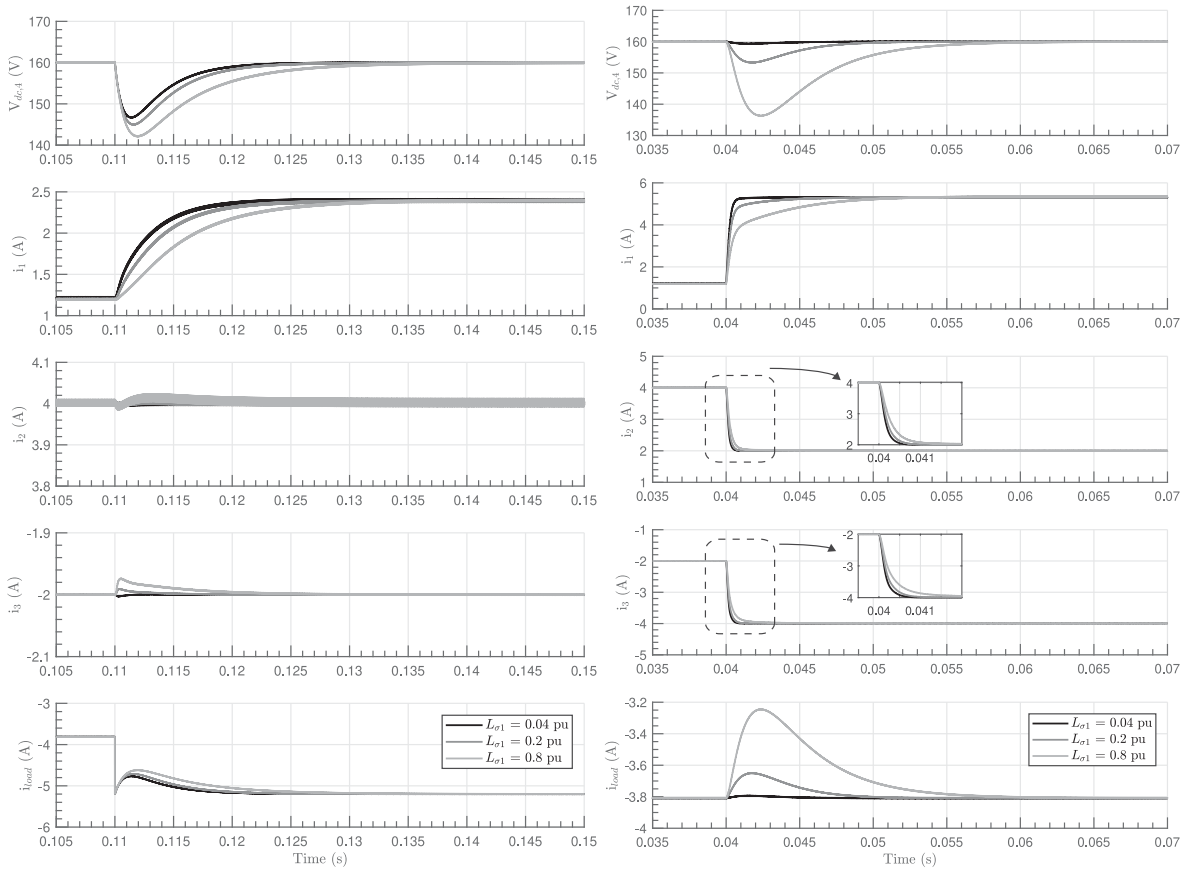

Fig. 10. Transient response of port voltages and currents at different master port leakage inductances during: (a) Case study I: A load step on load port #4 by switching a parallel resistor; (b) case study II: Simultaneous changes in the current set-points; 4 to 2 A for i^C2 and -2 to -4 A for i^C3. In both the case studies, port #1 acts as the slack bus.

thereby reducing the plant control to output gain; G_{44} in the small-signal gain matrix (27). Since the controller gains remain the same, the voltage restoration performance deteriorates.

Case Study II: At a certain time instant (t = 0.04 s), the current reference point in the source port #2 is changed from 4 to 2 A. Simultaneously, the current set-point in the load port #3 is changed from -2 to -4 A. Similar to the case study I, the simulations are repeated for different master port leakage port inductances. Fig. 10(b) shows the dynamic performance of the current loops and voltage loop of the ports around t = 0.04 s. The port #4 bus voltage disruption during the current set-point adjustments in the current-controlled ports is visible when the voltage drops by 24 V when the master port leakage inductance is 0.8 pu. Unlike the case study I, there is a significant interaction between the current and the voltage control loops. The slow voltage loop is not capable of rejecting the interference caused by the current set-points adjustments when the master port leakage inductances are 0.2 and 0.8 pu. However, when the

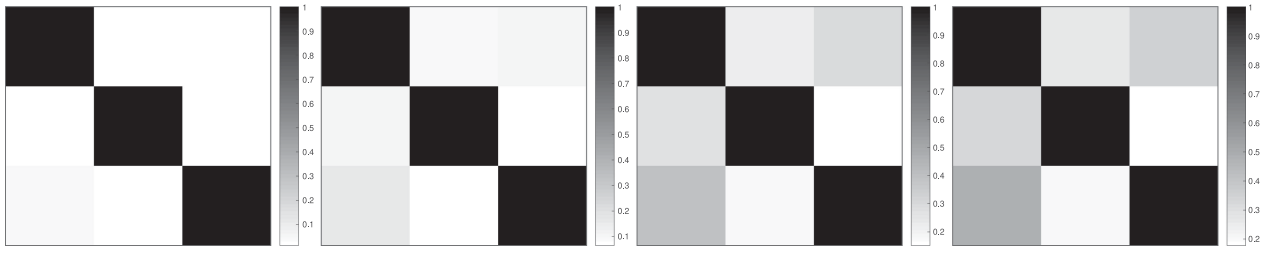

(a) (b) (c) (d)

Fig. 11. Two-dimensional (2-D) area plot of normalized gain matrix G_{norm} as expressed in (29) with master port leakage inductance $L_{\sigma 1}$. (a) 0.04 pu. (b) 0.2 pu. (c) 0.8 pu. (d) 1 pu.

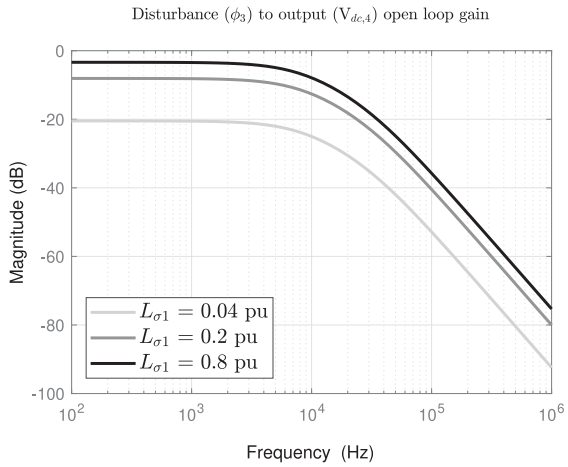

(a)

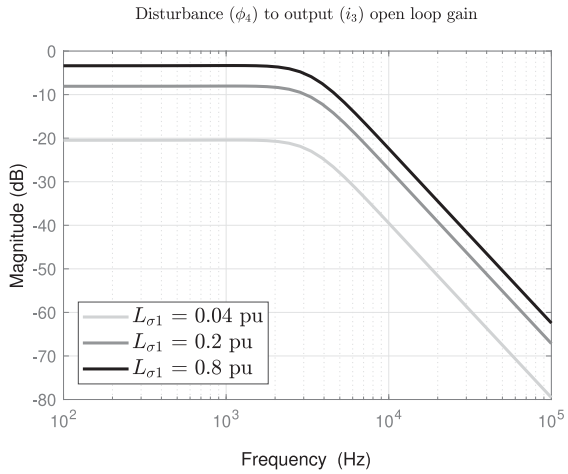

(b)

Fig. 12. Open loop response of disturbance to control output. (a) Current control variable ϕ_3 to voltage loop control output $V_{\text{dc},4}$. (b) Voltage control variable ϕ_4 to current loop control output i_3.

leakage inductance of the master port is 0.04 pu , the bus voltage disturbance is negligible.

The obtained simulation results can be explained by the analysis presented in Section II. At the end of the Section II-C, it was inferred that the degree of cross-coupling of the control loops is directly proportional to the relative value of the nondiagonal elements with the diagonal elements. To

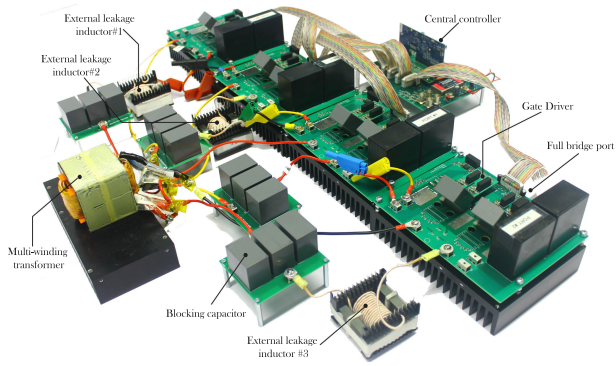

Fig. 13. QAB experimental laboratory prototype.

TABLE III
HF TRANSFORMER SPECIFICATIONS

Design parameter	Details
Core	2 stacks E-70/33/32
Material	N87 (EPCOS TDK)
Layer insulation	Kapton tape
Number of turns (N_1, N_2, N_3, N_4)	8,8,8,8
Parallel turns	4,2,2,2
Litz wire details	r_{strand} = 0.05 mm n_{strand} = 420
Leakage inductances (μH)	L_{12} = 8; L_{13} = 1.8; L_{14} = 6.7 L_{23} = 9; L_{34} = 9; L_{24} = 19

that end, the small signal gain matrix of the QAB converter as shown (27) is normalized as the following:

$$G_{\text{norm}} = \begin{bmatrix} 1 & \left|\frac{G_{23}}{G_{22}}\right| & \left|\frac{G_{24}}{G_{22}}\right| \\ \left|\frac{G_{32}}{G_{33}}\right| & 1 & \left|\frac{G_{34}}{G_{33}}\right| \\ \left|\frac{G_{42}}{G_{44}}\right| & \left|\frac{G_{43}}{G_{44}}\right| & 1 \end{bmatrix}. \tag{29}$$

Fig. 11 shows the area plot of the normalized gain matrix G_{norm} at different values of the master port leakage inductance. At $L_{\sigma 1} = 0.04$ pu, the matrix is essentially a diagonal matrix with the nondiagonal gain terms approaching zero. Nonetheless, as the leakage inductance reaches the base value of 1 pu, nondiagonal gain terms are increasingly comparable to diagonal terms leading to cross-coupling between control loops.

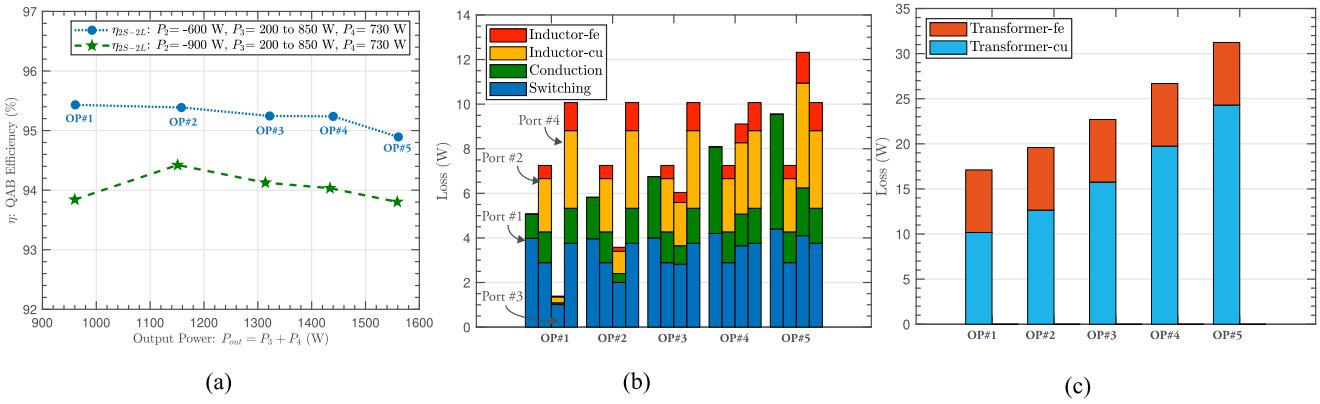

Fig. 14. (a) QAB converter efficiency during 2S-2 L mode of operation with two sources (ports #1 and #2) and two loads (ports #3 and #4). Port #3 acts as a variable load while port #1 acts as the slack port. Port #4 consumes a constant power of 730 W. Two sets of efficiency measurements are carried out with source port #2 supplying constant power of 600 and 900 W. (b) Loss distribution in different ports of the QAB converter at different operating points in 2S-2 L mode with P_3: 200 to 850 W (load), P_2: -600 W (source), and P_4: 730 W (load). (c) Loss distribution in the transformer of the QAB converter at different operating points.

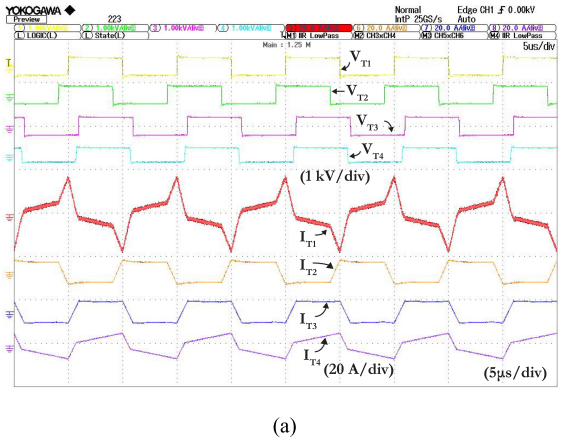

Fig. 15. (a) Steady-state waveforms of the transformer winding voltages and currents of the QAB converter in 2S-2 L mode at operating point #5. The inductor current shapes of the port inductor currents are similar to the theoretical waveforms presented in Fig. 7. (b) Thermal image of the QAB converter setup at OP #5 with highlighted hotspot temperatures.

In addition to the gain matrix approach, a disturbance to the output bode plot can be used to study the effect of the master port leakage inductance on the decoupling performance. Fig. 12(a) shows the disturbance (ϕ_3) to output ($V_{dc,4}$) bode plot for port #4.

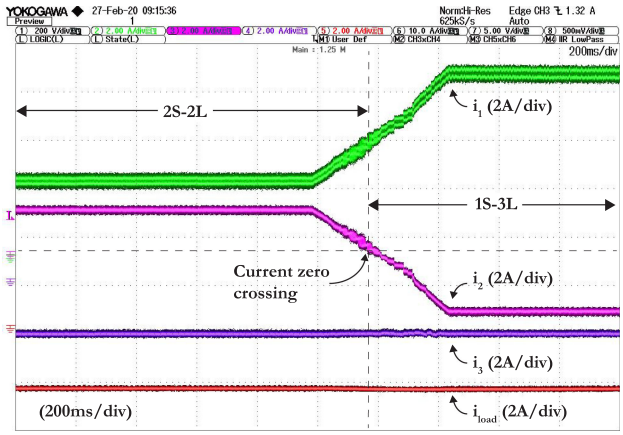

Fig. 16. Bidirectional power flow control in port #2 in the QAB converter prototype by ramping down the port power set-point. The converter mode of operation transitions from a 2S-2 L to a 1S-3 L.

Similarily, Fig. 12(b) depicts the disturbance (ϕ_4) to output (i_3) bode plot for port #3. All cases show that the low-frequency disturbance to output gain decreases by approximately 20 dB as the master port leakage inductance decreases from 0.8 to 0.04 pu. Therefore, when the master port leakage inductance is low ($\leq$0.05 pu), the PI controller gains of the individual control loops are sufficient to reject the cross-loop intereference. It must be noted that the above decoupling design criteria becomes difficult to achieve as the power rating and switching frequency of the MAB converter increases as the base inductance is inversely proportional to them as per (26).

In summary, the results of the simulation show that the proposed MAB configuration has inherently decoupled power flows if the master port leakage inductance is sufficiently low ($\leq$0.05 pu). In addition, it is shown that selecting different control bandwidths for the control loops in the MAB [15] does not guarantee power flow decoupling. The technique eliminates the noise due to the slower loop on the faster loop. However the slower control loop becomes more vulnerable to disruption caused by faster control loops.

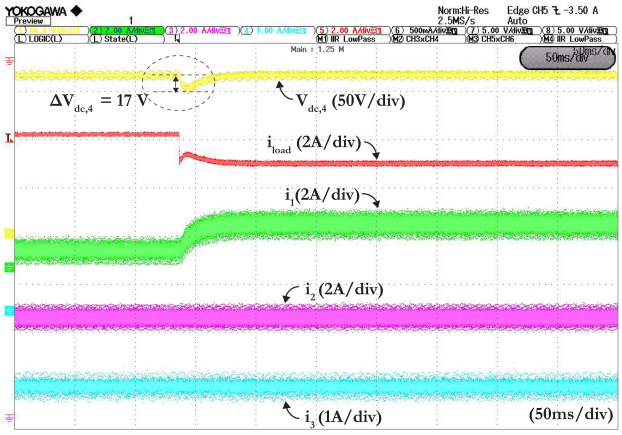

(a)

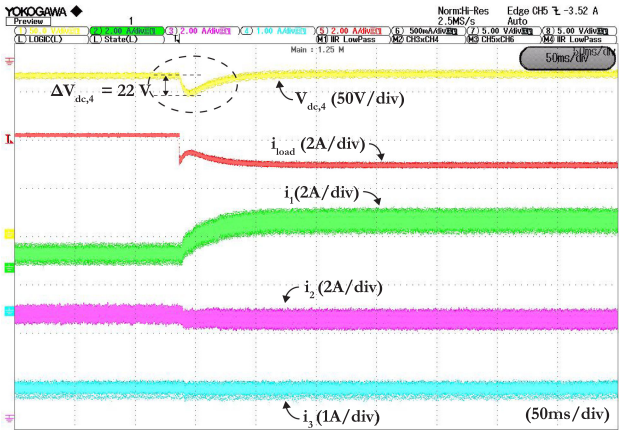

(b)

Fig. 17. Transient behavior of the control currents and voltage during a load step of QAB system configuration. (a) $L_{\sigma 1} = 0$ pu. (b) $L_{\sigma 1} = 0.6$ pu.

V. Experimental Results

Experiments are performed on a QAB converter prototype to demonstrate the inherently decoupled flow control of the proposed MAB configuration. To that end, the overall experimental setup, along with the system components, is addressed in the next segment. Additionally, the efficiency of operation and distribution of losses are presented. The dynamic decoupling performance of the QAB converter prototype is presented at the end.

A. QAB Components and Laboratory Setup

The experimental QAB prototype is identical to the simulation schematic (Fig. 8) without the dc-side filter inductors with all other parameters remaining the same (Table II). The laboratory QAB converter setup is presented in Fig. 13. The overall system consists of four full-bridge modules connected via a high-frequency multiwinding transformer with three bidirectional dc power supplies (SM 500 CP-90 Delta Elektronika) and a resistive load of 35 Ω. Si-C MOSFETs (Wolfspeed C3M0065100 K) are used for the full-bridge modules. Three external leakage inductors of value 25 μH for the three slave ports are highlighted in Fig. 13. Blocking capacitors are connected to each transformer winding to ensure the transformer is not saturated due to dc bias during transient and steady-state operating conditions. The central controller is implemented on a Texas Instruments TMS320F28379D DSP. The HF transformer is implemented by using two stacks of E-70/33/32 cores (core material N87) in parallel. The transformer windings are interleaved to ensure low leakage inductance of the windings. Leakage impedance tests on the HF transformer are conducted to evaluate the interwinding leakage inductances. Table III presents the design specifications of the HF transformer along with the experimentally obtained values of the leakage inductances of the delta-equivalent circuit. The transformer winding #1 is designed to have the lowest leakage among all the windings, as evident from the experimentally obtained leakage inductance values in Table III. Therefore, the port connected to the winding #1 is used as the master port.

B. Efficiency and Distribution of Losses

The efficiency of the QAB converter prototype is experimentally measured using Yokogawa WT500 power analyzer. The QAB converter efficiency is measured with two sources (ports #1 and #2) and two loads (ports #3 and #4). The power of the load port #4 is kept constant at 730 W, whereas the load power at port #3 is varied from 200 to 850 W. Two sets of experiment with the above power loading are conducted: 1) port #2 supplies constant power at 600 W, and 2) port #2 supplies constant power at 900 W. Fig. 14(a) shows the measured efficiency curves obtained from the experiments. The QAB efficiency curve obtained during port #3 supplying power of 600 W is higher compared to the case during port #3 supplying power of 900 W by 1%–1.5%. Unequal sharing of the power between port #1 and #2 results in higher losses in the second case ($P_2 = -900$ W).

The operating points in the first set of experiments (OP#1 - OP#5) are modelled to analyze the loss distribution within the QAB converter. Fig. 14(b) shows the losses incurred at different ports of the QAB converter as the load power P_3 is increased. It can be observed from the loss distribution that the MOSFET conduction losses in both port #1 and port #3 increase as they process more power from operating point 1 to 5. Similarly, the MOSFET switching losses in port #3 increase as the power increases. In all the operating points, port #3 MOSFETs are soft-switched. Therefore, they have zero turn-ON losses. As the peak current during turning-OFF increases with increasing power, the turn-OFFlosses of the port #3 MOSFETs increase. However, the MOSFET switching losses in port #1 almost remain constant even though the power delivered increases. Similar to port #3, the MOSFETs in port #1 are also soft-switched leading to zero turn-ON losses. However, due to low leakage inductance of the master port, the peak current (i_{T1}) during the turn-OFFtransition is high as seen in the steady-state transformer waveforms shown in Fig. 15(a). The master port inductor peak current value doesn't increase significantly as the power delivered by the master port increases. Therefore, the MOSFET switching losses in port #1 remain constant. The high peak transformer current of the master port in the proposed MAB configuration results in high turn-OFFswitching losses irrespective of operating point.

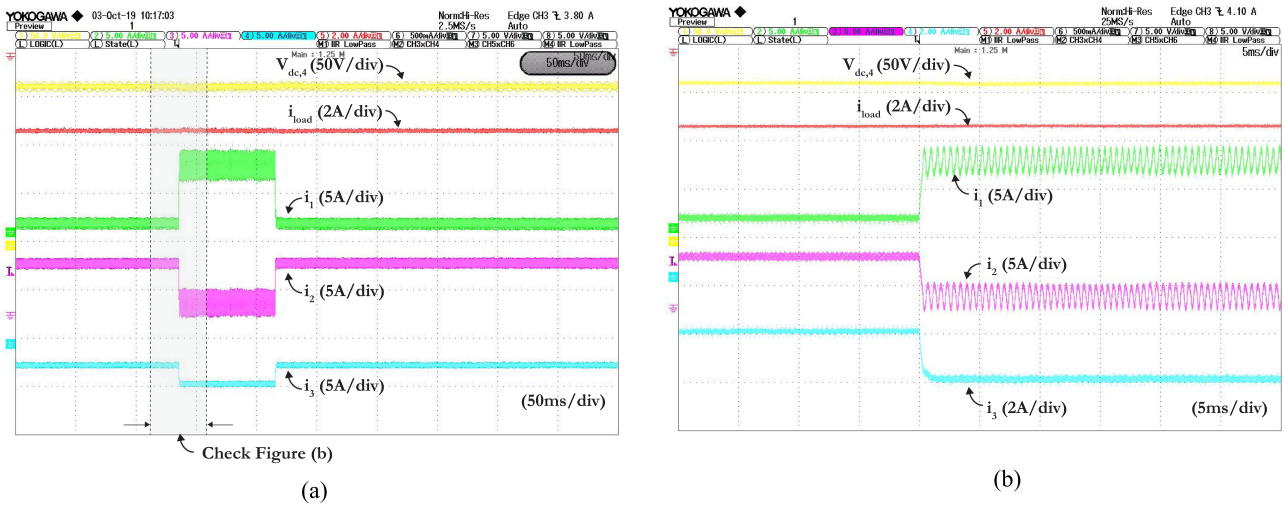

Fig. 18. Dynamic performance of the control currents and voltage during set-point alterations in port #2 and port #3 with QAB configuration with $L_{\sigma 1} = 0$ pu. The current set point in port #2 is changed from 4 to 2 A and back to 4 A. The current set point in port #3 is changed from -2 to -4 A and back to -2 A. (a) Overall transient waveforms. (b) Transient waveforms during the first set-point change.

This is a drawback of the proposed configuration compared to the conventional configuration.

The transformer loss distribution is presented in Fig. 14(c). The winding losses increase as the overall power processed by the QAB converter increases from operation point #1 to point #5. However, the core losses remain constant independent of the power processed by the transformer. Due to the zero leakage inductance, only the master port volt-seconds determine the flux density swing in the transformer. Since the master port volt-seconds remain constant throughout the operating points, the core losses also remain the same. Finally, Fig. 15(b) shows the thermal performance of the QAB converter at operating point #5.

C. Dynamic Behavior and Decoupling Validation

The dynamic characteristics of the QAB converter prototype is presented here. As highlighted previously, one of the significant advantages of the MAB converter family is the capability of controlling the power of ports in both directions. Fig. 16 demonstrates a case study where the power in port #2 is controlled in both directions. The port #2 current alters direction tracking the ramped power set-point. It can be further observed that port #1 acts as the slack port of the converter as the QAB converter transitions from a 2S-2 L mode of operation to a 1 source–3 load (1S-3 L) mode. Thus, the bidirectional power flow control of the QAB converter is validated.

The power flow dynamic decoupling performance of the proposed QAB converter is validated by performing multiple experiments on the prototype. The experiments are divided into two case studies similar to the simulations in Section IV-B.

1) A step load in the load port #4 to investigate the effect of the relatively slower voltage loop on the current loops in ports #2 and #3.
2) Simultaneous step change of current set points in ports #2 and #3 to study the effect of the current loops on the efficacy of the voltage control loop in port #4.

In addition, two sets of experiments are carried out: 1) the conventional QAB configuration with an external inductor of $L_{\sigma 1} = 0.6$ pu is connected to the slack port winding transformer, and 2) the proposed QAB configuration without an external inductor as a leakage inductance connected to the slack port winding transformer. The results obtained from the two configurations are compared to evaluate the effectiveness of the proposed configuration in terms of power flow decoupling.

The load step is realized on port #4 by switching a resistive load of 130 Ω in parallel with an existing load of 35 Ω. The dynamic behavior of the converter port currents and voltages is shown in Fig. 17. Fig. 17(a) shows that the port currents of ports #2 and #3 are not affected by the load step change in port #4 when there is no external leakage inductance added to the slack port transformer windings ($L_{\sigma 1} = 0$ pu). The voltage dip at the load dc bus is 17 V. In case of the conventional QAB configuration ($L_{\sigma 1} = 0.6$ pu), the load port voltage dip is approximately 22 V. Simulation findings have also shown similar behavior as reported in Fig. 10(a). The cross-loop interference generated by the voltage loop is corrected by faster current loops regardless of the leakage inductance of the master port. In conclusion, the proposed QAB configuration has faster voltage restoration performance during load step compared to the conventional QAB configuration. However, in both the configurations the cross-coupling effect of the slower voltage loop on the current loops is negligible.

The interference due to the current control loops on the voltage loop obtained from the experimental results is studied in this section. The current reference points at ports #2 and #3 are changed simultaneously ($I_{2,\text{set-point}} = 4$ to 2 to 4 A, $I_{3,\text{set-point}} = -2$ to -4 to -2 A). The transient response of the dc bus voltage during this event is observed for both the converter configurations with and without external leakage inductances. Figs. 18 and 19 show the transient behavior of the load dc bus voltage and the controlled currents of the proposed QAB configuration ($L_{\sigma 1} = 0$ pu) and the conventional QAB configuration ($L_{\sigma 1} = 0.6$ pu), respectively. The full decoupling of the control loops is observed

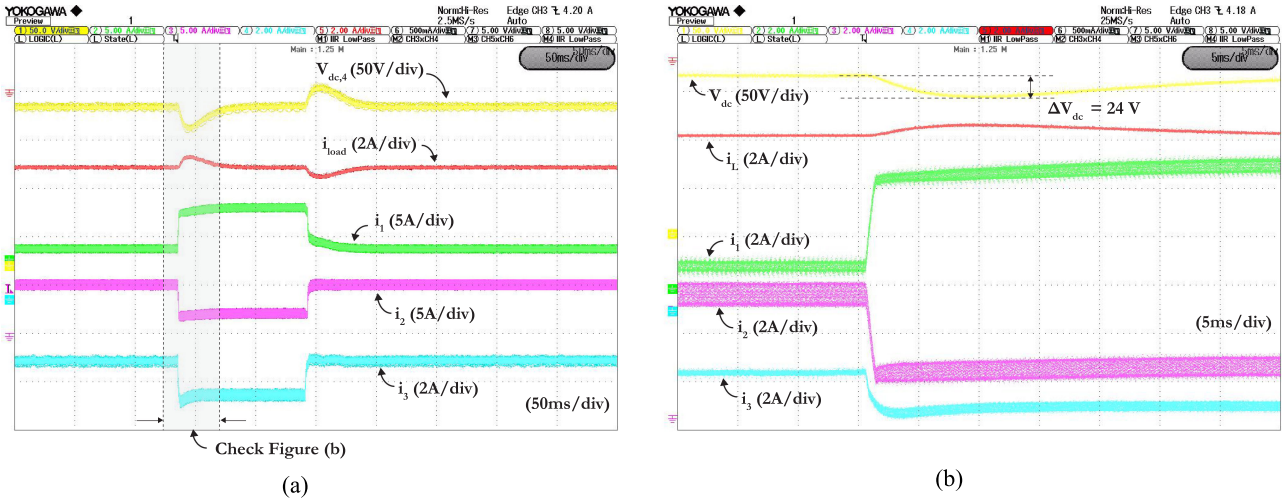

Fig. 19. Dynamic performance of the control currents and voltage during set-point alterations in port #2 and port #3 with QAB configuration with $L_{\sigma 1} = 0.6$ pu. The current set point in port #2 is changed from 4 to 2 A and back to 4 A. The current set point in port #3 is changed from -2 to -4 A and back to -2 A. (a) Overall transient waveforms. (b) Transient waveforms during the first set-point change.

from Fig. 18(a) without any disruption to the dc bus voltage due to the current loop control operation. However, in case of the conventional converter configuration ($L_{\sigma 1} = 0.6$ pu), the dc bus voltage is affected by the control action in the current control loops in as shown in Fig. 19. Fig. 19(b) shows that the dc bus voltage drops approximately 24 V (15% of the nominal bus voltage) during the current set-point changes in port #2 and port #3 before the voltage control restores the dc bus nominal voltage. Similar results are obtained by simulation in Section IV-B. In conclusion, the proposed QAB configuration shows complete dynamic decoupling of the control loops independent of individual control bandwidths.

VI. Conclusion

The main challenge of MAB converter design is to control the power flow between different sources in a highly coupled multiwinding transformer resulting in a coupled MIMO system. The contribution of this article is the proposed MAB converter configuration with magnetically decoupled power flows, which enables the regulation of power flows independently of the controller bandwidth. The MAB configuration is based on making a port with low leakage inductance ($\leq$ 0.05 pu) act as a rigid-voltage source on the transformer magnetizing inductance while adding external inductors (1 pu) to the rest of the ports. Simulations show that the proposed configuration decomposes the MIMO system into independent SISO systems with no mutual interaction. Experiments carried out on a 2-kW, 100-kHz four-port MAB converter laboratory prototype verify the converter operation and decoupled power flow control. In summary, the proposed design solves the problem of power flow coupling inherent to MAB converters without losing any advantage of the MAB converter family. Thus, it allows an increase in the number of ports without increased control complexity leading to higher system reliability and robustness. However, the decoupling condition slightly increases the design complexity of the multiwinding transformer. In conclusion, the MAB converter with the proposed configuration is highly attractive to a wide range of applications requiring interfacing of multiple dc sources like rooftop PV, storages, and loads with galvanic isolation. The effect of the asymmetrical leakage inductance distribution on the soft-switching boundaries of the MAB converter is an interesting direction for future research.

References

[1] A. K. Bhattacharjee, N. Kutkut, and I. Batarseh, "Review of multiport converters for solar and energy storage integration," *IEEE Trans. Power Electron.*, vol. 34, no. 2, pp. 1431–1445, Feb. 2019.

[2] P. Wheeler and S. Bozhko, "The more electric aircraft: Technology and challenges," *IEEE Electrific. Mag.*, vol. 2, no. 4, pp. 6–12, Dec. 2014.

[3] G. Sulligoi, A. Vicenzutti, and R. Menis, "All-electric ship design: From electrical propulsion to integrated electrical and electronic power systems," *IEEE Trans. Transp. Electrific.*, vol. 2, no. 4, pp. 507–521, Dec. 2016.

[4] G. Buticchi, L. F. Costa, D. Barater, M. Liserre, and E. D. Amarillo, "A quadruple active bridge converter for the storage integration on the more electric aircraft," *IEEE Trans. Power Electron.*, vol. 33, no. 9, pp. 8174–8186, Sep. 2018.

[5] H. Chen, Z. Hu, H. Luo, J. Qin, R. Rajagopal, and H. Zhang, "Design and planning of a multiple-charger multiple-port charging system for pev charging station," *IEEE Trans. Smart Grid*, vol. 10, no. 1, pp. 173–183, Jan. 2019.

[6] M. Vasiladiotis and A. Rufer, "A modular multiport power electronic transformer with integrated split battery energy storage for versatile ultrafast ev charging stations," *IEEE Trans. Ind. Electron.*, vol. 62, no. 5, pp. 3213–3222, May 2015.

[7] J. Schäfer, D. Bortis, and J. W. Kolar, "Multi-port multi-cell dc/dc converter topology for electric vehicle's power distribution networks," in *Proc. IEEE 18th Workshop Control Model. Power Electron.*, 2017, pp. 1–9.

[8] S. Falcones, R. Ayyanar, and X. Mao, "A DC–DC multiport-converter-based solid-state transformer integrating distributed generation and storage," *IEEE Trans. Power Electron.*, vol. 28, no. 5, pp. 2192–2203, May 2013.

[9] C. Zhao and J. W. Kolar, "A novel three-phase three-port ups employing a single high-frequency isolation transformer," in *Proc. Power Electron. Specialists Conf.*, 2004, vol. 6, pp. 4135–4141.

[10] H. Krishnaswami and N. Mohan, "Three-port series-resonant DC–DC converter to interface renewable energy sources with bidirectional load and energy storage ports," *IEEE Trans. Power Electron.*, vol. 24, no. 10, pp. 2289–2297, Oct. 2009.

[11] E. Asa, K. Colak, M. Bojarski, and D. Czarkowski, "Asymmetrical duty-cycle and phase-shift control of a novel multiport CLL resonant converter," *IEEE J. Emerg. Sel. Topics Power Electron.*, vol. 3, no. 4, pp. 1122–1131, Dec. 2015.
[12] Y. Chen, P. Wang, H. Li, and M. Chen, "Power flow control in multi-active-bridge converters: Theories and applications," in *Proc. IEEE Appl. Power Electron. Conf. Expo.*, 2019, pp. 1500–1507.
[13] R. W. De Doncker, D. M. Divan, and M. H. Kheraluwala, "A three-phase soft-switched high-power-density DC/DC converter for high-power applications," *IEEE Trans. Ind. Appl.*, vol. 27, no. 1, pp. 63–73, Jan./Feb. 1991.
[14] C. Zhao, S. D. Round, and J. W. Kolar, "An isolated three-port bidirectional DC–DC converter with decoupled power flow management," *IEEE Trans. Power Electron.*, vol. 23, pp. 2443–2453, Sep. 2008.
[15] H. Tao, A. Kotsopoulos, J. Duarte, and M. Hendrix, "A soft-switched three-port bidirectional converter for fuel cell and supercapacitor applications," in *Proc. IEEE 36th Power Electron. Specialists Conf.*, 2005, pp. 2487–2493.
[16] L. Wang, Z. Wang, and H. Li, "Asymmetrical duty cycle control and decoupled power flow design of a three-port bidirectional DC–DC converter for fuel cell vehicle application," *IEEE Trans. Power Electron.*, vol. 27, no. 2, pp. 891–904, Feb. 2012.
[17] H. Matsuo, W. Lin, F. Kurokawa, T. Shigemizu, and N. Watanabe, "Characteristics of the multiple-input DC–DC converter," *IEEE Trans. Ind. Electron.*, vol. 51, no. 3, pp. 625–631, Jun. 2004.
[18] P. Wang, X. Lu, W. Wang, and D. Xu, "Hardware decoupling and autonomous control of series-resonance-based three-port converters in DC microgrids," *IEEE Trans. Ind. Appl.*, vol. 55, no. 4, pp. 3901–3914, Jul./Aug. 2019.
[19] L. F. Costa, G. Buticchi, and M. Liserre, "Quad-active-bridge DC–DC converter as cross-link for medium-voltage modular inverters," *IEEE Trans. Industry Appl.*, vol. 53, pp. 1243–1253, Mar./Apr. 2016.
[20] R. W. Erickson and D. Maksimovic, *Fundamentals of Power Electronics*. Berlin, Germany: Springer, 2007.
[21] R. D. Middlebrook and S. Cuk, "A general unified approach to modelling switching-converter power stages," in *Proc. IEEE Power Electron. Specialists Conf.*, 1976, pp. 18–34.
[22] H. Bai, C. Mi, C. Wang, and S. Gargies, "The dynamic model and hybrid phase-shift control of a dual-active-bridge converter," in *Proc. Annu. Conf. IEEE Ind. Electron.*, 2008, pp. 2840–2845.
[23] K. Zhang, Z. Shan, and J. Jatskevich, "Large-and small-signal average-value modeling of dual-active-bridge DC–DC converter considering power losses," *IEEE Trans. Power Electron.*, vol. 32, no. 3, pp. 1964–1974, Mar. 2017.
[24] V. Vorpérian, "Simplified analysis of PWM converters using model of PWM switch Part II: Discontinuous conduction mode," *IEEE Trans. Aerosp. Electron. Syst.*, vol. 26, no. 3, pp. 497–505, May 1990.
[25] P. Wang, Y. Chen, Y. Elasser, and M. Chen, "Small signal model for very-large-scale multi-active-bridge differential power processing (MAB-DPP) architecture," in *Proc. 20th Workshop Control Model. Power Electron.*, 2019, pp. 1–8.
[26] Q.-G. Wang, *Decoupling Control*, vol. 285. Berlin, Germany: Springer, 2002.

Soumya Bandyopadhyay (Student Member, IEEE) received the B.Tech. degree (first class hons.) in electrical and electronics engineering from the Jadavpur University, Kolkata, India, in 2011, and the M.Sc. degree in electrical engineering in 2015 from the Delft University of Technology, Delft, The Netherlands, where he is currently working toward the Ph.D. degree in key power electronics in low voltage dc distribution systems.

His research interests include design and control of multiport dc–dc converter design for renewable sources and storages, smart charging of electric vehicles, and wireless power transfer.

Pavel Purgat (Student Member, IEEE) received the B.Sc. degree in electrical engineering from the Czech Technical University, Prague, Czech Republic, in 2014 and the M.Sc. degree in electrical engineering, with focus on power electronics and inductive power transfer control, in 2016 from the Delft University of Technology, Delft, Netherlands, where he is currently working toward the Ph.D. degree.

In 2017, he was a Visiting Researcher with the Fraunhofer-IISB, Erlangen, Germany. In 2020, he joined the Eaton Industries GmbH in Vienna, Austria. His research interests include power electronics and power electronics intensive applications.

Zian Qin (Senior Member, IEEE) received the B.Eng. degree in automation from Beihang University, Beijing, China, in 2009, the M.Eng. degree in control science and the engineering from Beijing Institute of Technology, Beijing, China, in 2012, and the Ph.D. degree from Aalborg University, Aalborg, Denmark, in 2015.

He is currently an Assistant Professor with the Delft University of Technology, Delft, Netherlands. In 2014, he was a Visiting Scientist with Aachen University, Aachen, Germany. From 2015 to 2017, he was a Postdoctoral Research Fellow with Aalborg University. His research interests include wide bandgap devices, power electronics based grid, and Power2X.

Dr. Qin serves as the Technical Programme Chair of the IEEE-International Symposium on Industrial Electronics (ISIE) 2020, Technical Program Co-Chair of the IEEE-Workshop on Control and Modeling for Power Electronics (COMPEL) 2020, Industrial Session Co-Chair of the Energy Conversion Congress and Exposition (ECCE)-Asia 2020.

Pavol Bauer (Senior Member, IEEE) received the master's degree in electrical engineering from the Technical University of Kosice, Koice, Slovakia, in 1985, and the Ph.D. degree from the Delft University of Technology, Delft, The Netherlands, in 1995.

He is currently a Full Professor with the Department of Electrical Sustainable Energy, Delft University of Technology, and the Head of DC Systems, Energy Conversion and Storage Group. He received the title of Professor from the president of Czech Republic at the Brno University of Technology in 2008 and at the Delft University of Technology in 2016. He has worked on many projects for industry concerning wind and wave energy, power electronic applications for power systems such as Smarttrafo; HVdc systems, projects for smart cities such as PV charging of electric vehicles, PV and storage integration, contactless charging. He has also participated in several Leonardo da Vinci and H2020 EU projects as Project Partner (ELINA, INETELE, E-Pragmatic) and Co-ordinator (PEMCWebLab.com-Edipe, SustEner, Eranet DCMICRO). He has authored or coauthored over 72 journal and almost 300 conference papers (with H factor Google Scholar 43, Web of Science 20). He has also authored or co-authored eight books, holds four international patents, and organized several tutorials at several international conferences.